

Raman scattering under extreme conditions

Feng Jin(金峰), Yang Yang(杨洋), An-Min Zhang(张安民), Jian-Ting Ji(籍建葶), Qing-Ming Zhang(张清明)

Citation: Chin. Phys. B . 2018, 27(7): 077803. **doi:** 10.1088/1674-1056/27/7/077801

Journal homepage: http://cpb.iphy.ac.cn; http://iopscience.iop.org/cpb

What follows is a list of articles you may be interested in

A general method for large-scale fabrication of Cu nanoislands/dragonfly wing SERS flexible substrates

Yuhong Wang(王玉红), Mingli Wang(王明利), Lin Shen(沈琳), Yanying Zhu(朱艳英), Xin Sun(孙鑫), Guochao Shi(史国超), Xiaona Xu(许晓娜), Ruifeng Li(李瑞峰), Wanli Ma(马万里)

Chin. Phys. B . 2018, 27(1): 017801. **doi:** 10.1088/1674-1056/27/1/017801

Different angle-resolved polarization configurations of Raman spectroscopy: A case on the basal and edge plane of two-dimensional materials

Xue-Lu Liu(刘雪璐), Xin Zhang(张昕), Miao-Ling Lin(林妙玲), Ping-Heng Tan(谭平恒)

Chin. Phys. B . 2017, 26(6): 067802. **doi:** 10.1088/1674-1056/26/6/067802

Raman scattering studies on the collapsed phase of $CaCo_2As_2$

Jianting Ji(籍建葶), Anmin Zhang(张安民), Run Yang(杨润), Yong Tian(田勇), Feng Jin(金峰), Xianggang Qiu(邱祥冈), Qingming Zhang(张清明)

Chin. Phys. B . 2016, 25(6): 067803. **doi:** 10.1088/1674-1056/25/6/067803

High-temperature Raman spectroscopic study of vanadoborate $Na_3VO_2B_6O_{11}$

Ji Zhang(张季), De-Ming Zhang(张德明), Qing-Li Zhang(张庆礼), Shao-Tang Yin(殷绍唐)

Chin. Phys. B . 2016, 25(3): 037802. **doi:** 10.1088/1674-1056/25/3/037802

Elastic, dielectric, and piezoelectric characterization of $0.92Pb(Zn_{1/3}Nb_{2/3})O_3$-$0.08PbTiO_3$ single crystal by Brillouin scattering

Fang Shao-Xi, Tang Dong-Yun, Chen Zhao-Ming, Zhang Hua, Liu Yu-Long

Chin. Phys. B . 2015, 24(2): 027802. **doi:** 10.1088/1674-1056/24/2/027802

TOPICAL REVIEW — Synergetic Extreme Condition User Facility: Breakthroughs and opportunities for the research of physical science

Raman scattering under extreme conditions*

Feng Jin(金峰)[1], Yang Yang(杨洋)[2], An-Min Zhang(张安民)[1], Jian-Ting Ji(籍建葶)[1,2], and Qing-Ming Zhang(张清明)[1,2,3,†]

[1] *Department of Physics, Renmin University of China, Beijing* 100872, *China*
[2] *Beijing National Laboratory for Condensed Matter Physics, Institute of Physics, Chinese Academy of Sciences, Beijing* 100190, *China*
[3] *School of Physical Science and Technology, Lanzhou University, Lanzhou* 730000, *China*

(Received 3 April 2018; revised manuscript received 24 April 2018; published online 25 June 2018)

Raman scattering is a versatile and powerful technique and has been widely used in modern scientific research and vast industrial applications. It is one of the fundamental experimental techniques in condensed matter physics, since it can sensitively probe the basic elementary excitations in solids like electron, phonon, magnon, etc. The application of extreme conditions (low temperature, high magnetic field, high pressure, etc.) to Raman scattering, will push its capability up to an unprecedented level, because this enables us to look into new quantum phases driven by extreme conditions, trace the evolution of the excitations and their coupling, and hence uncover the underlying physics. This review contains two topics. In the first part, we will introduce the Raman facility under extreme conditions, belonging to the optical spectroscopy station of Synergetic Extreme Condition User Facilities (SECUF), with emphasis on the system design and the capability the facility can provide. Then in the second part we will focus on the applications of Raman scattering under extreme conditions to a variety of condensed matter systems such as superconductors, correlated electron systems, charge density waves (CDW) materials, etc. Finally, as a rapidly developing technique, time-resolved Raman scattering will be highlighted here.

Keywords: Raman scattering technique, extreme conditions, correlated electron systems, time-resolved Raman scattering

PACS: 78.30.–j, 07.55.Db, 71.27.+a, 78.47.je **DOI:** 10.1088/1674-1056/27/7/077801

1. Introduction

Raman scattering is an inelastic light scattering process, i.e., one photon in one photon out. The differences in momentum and energy between incident and scattered photons are transferred to sample and excite quasiparticles in solids. It is basically analogical to inelastic neutron scattering. In fact, both processes share the similar phenomenological description. The Raman effect was discovered in 1928 by Raman. It is a quite tiny and subtle light scattering effect, and is usually over five orders of magnitude smaller than elastic scattering in intensity. In the early stage of Raman scattering history, it is hard to observe the effect due to the lack of high-gain detectors, particularly high-intensity light sources. The invention of laser in 1960s thoroughly changes the situation. The significant progresses in detectors (charge-coupled devices), holographic gratings, and other optical/electronic aspects, eventually push this technique to become a popular experimental tool in modern scientific research and industrial applications. Besides the conventional one, many technical branches such as resonant Raman scattering, tip-enhanced Raman scattering, surface-enhanced Raman scattering, time-resolved Raman scattering, etc., have been extensively developed in the last few decades. All these branches contribute to form a large Raman scattering family nowadays.

In most of the extensive applications, Raman scattering is employed as a fast, convenient, and non-destructive sample-characterization tool, just like x-ray diffraction. On the other hand, Raman scattering plays a vital role in the fundamental research, particularly in the vast field of condensed matter physics. Unlike many other techniques, Raman can probe various excitations from different degrees of freedom, as incident light is an optical-frequency electromagnetic radiation which easily interacts with substance. Basically, the so-called extreme conditions such as low temperature, high pressure, high magnetic field, ultrafast process, etc., can drive condensed matter into new quantum phases in which the novel excitations may be found and the exciting new physics may be established. Thus, Raman technique combined with extreme conditions is expected to tell us new knowledge of novel states of matter and bring us into a colorful physics world.

The review contains five sections and is organized as follows. We give a short introduction to Raman scattering in the

*Project supported by the Ministry of Science and Technology of China (Grant Nos. 2016YFA0300504 and 2017YFA0302904) and the National Natural Science Foundation of China (Grant Nos. 11474357, 11774419, 11604383, and 11704401). Y. Y. was supported by the Scientific Equipment Development Project of Chinese Academy of Sciences (Grant No. YJKYYQ20170027).

†Corresponding author. E-mail: qingmingzhang@gmail.com

© 2018 Chinese Physical Society and IOP Publishing Ltd

first section. In Section 2, we will introduce the Raman facility under extreme conditions of SECUF in detail. And the applications of Raman scattering under extreme conditions to many real systems will be discussed in Section 3. In Section 4, we will single out time-resolved Raman scattering, a unique and fast-developing Raman branch, to take a glance at its interesting applications when combined with extreme conditions. And finally, we will give a brief summary.

2. Raman facility of SECUF

As a long-term national strategy aiming at the frontiers in condensed matter physics and material science, SECUF involves various top experimental techniques under extreme conditions. Raman facility is one of the key facilities of the optical spectroscopy station.

There are several guiding principles for designing such a Raman system. First, the system needs to highlight the feature of extreme conditions. It means that the system works not only in a single extreme condition. In some cases, we need to make Raman measurements under multiple extreme conditions combined together. For instance, usually we can collect Raman spectra at different temperatures and make a careful analysis on temperature dependence of one or more modes. On the other hand, it is also possible that the novel phases or excitations we are interested in, may be hidden behind more extreme conditions, not only low temperatures. In these cases, we have to simultaneously employ multi-extreme conditions like low temperatures, high magnetic fields, high pressure, etc., to probe unusual excitations. The simultaneous application of multi-extreme conditions will perhaps be a big challenge for Raman measurements, since Raman signal in this case may be dramatically reduced. This requires a careful and thorough optimization for the optical components along laser beam path. Second, the rapid development in optics and electronics is changing and shaping the future of Raman technique. Some of the important progresses in recent years should be reflected in the system. These include volume Bragg gratings, high-sensitivity detectors, broadband white laser sources, time-resolved measurement technique, etc. The system should also preserve the interfaces for future extensions, like tip/surface enhanced Raman scattering. Finally, this is a facility for the users worldwide, not just a laboratory setup for one or two professional groups. The efficiency, ease of use, maintainability, and extendibility of the system are real concerns and should be taken into account.

The sketch drawing of the Raman facility is shown in Fig. 1. The whole system can be roughly divided into three subsystems, i.e., light source subsystem, continuous-wave (CW) Raman system, and time-resolved Raman subsystem. The light source subsystem includes single-frequency DPSS lasers with different output wavelengths, broadband white laser source, and ultrafast laser. It is an exchangeable and flexible design and the two Raman subsystems can share the light sources through switch-optics or optical fiber.

There are some reasons for employing double Raman subsystems for the facility. One important reason is to guarantee the facility efficiency. Time-resolved Raman measurement is a very time-consuming work. Integration of multiple extreme conditions makes it much harder. If there is only one spectrometer, which could be occupied by time-resolved measurements for a long period, the requests for continuous-wave Raman measurements will be seriously blocked. As mentioned above, the two subsystems can share the light sources. They are complementary in this sense.

According to the frequently-used light sources, the two Raman subsystems are defined as continuous-wave and time-resolved subsystems, respectively. We will have detailed descriptions for them in the following.

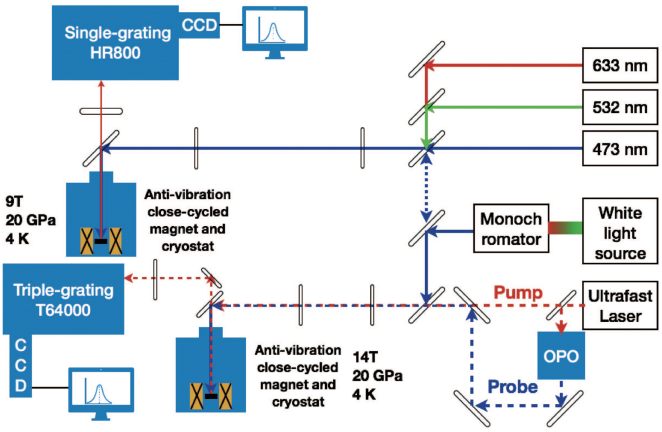


Fig. 1. (color online) Schematic diagram of SECUF Raman facility. The light sources include solid state lasers with different wavelengths, broadband white light source, and ultrafast laser. A single-grating spectrometer and a triple-grating spectrometer are adopted. The sample environments are achieved using anti-vibration close-cycled magnet and cryostat.

2.1. Continuous-wave Raman subsystem

With this subsystem, one can make conventional Raman measurements under low temperature (4 K), magnetic field (9 T), and high pressure (20 GPa). The vertical backscattering configuration is adopted to fit the magnet and cryostat.

Light source. Single-frequency solid state lasers are employed for the subsystem. The wavelengths sparsely cover the visible range from red to blue. This enables to check the photoluminescence effect and do some resonance Raman studies. In some particular cases, Raman signal strongly depends on the wavelength of incident light and the optional wavelengths will be very helpful in such cases. The incident laser beam passes through a pair of Bragg gratings which can filter out the unwanted lines generated in the optical cavity and guarantee a clean laser line with a narrow linewidth.

Spectrometer. Single-grating monochromator (Jobin Yvon HR800) is used in the subsystem. The spectral reso-

lution is ~ 1.2 cm^{-1} at 633 nm. Compared to the double- or triple-grating one, it provides a good balance between efficiency and performance. The application of the suite of volume Bragg grating can push the measurable lowest wavenumbers down to 5–10 cm^{-1}. The spectrometer is equipped with a liquid-nitrogen-cooled and back-illuminated CCD.

Magnet and cryostat. Sample environments or extreme conditions are provided by a close-cycled magnet and cryostat system which integrates low temperatures down to 4 K and magnetic fields up to 9 T. The system takes an anti-vibration design to avoid the vibration generated by the refrigerator. A customized optical insert is used to couple the incident light/the scattered light in/out of the cryostat. The customized objective lens is made of non-magnetic and low-thermal-expansion materials since it is placed inside the cryostat and the magnet. The application of high pressure together with low temperatures and high magnetic fields is a real challenge. Both the magnet bore diameter and the working distance of the objective lens strongly limit the size of the diamond anvil cell. It means that for the magnet and cryostat, we need to customize a pressure cell as small as possible.

Precise positioning and rotating stages. For a microscopic Raman measurement, an XYZ-stage with a resolution of $\sim$ μm is very helpful to select an optimal focus spot and compensate the drift of the focus spot when varying temperatures. A precise sample positioning mechanism, which is also made of non-magnetic and low-thermal-expansion materials for the same reason as mentioned above, is applied in the cryostat and magnet. The sample positioner is an XYZ-stage driven by piezoelectric actuators (attoCube). Symmetry analysis is one of the unique and powerful functions of Raman scattering. For this purpose, a piezo-driven rotator mounted on the positioner will allow us to conveniently make rotation measurements under extreme conditions. It would be particularly useful for studying structural phase transitions or symmetry breaking.

2.2. Time-resolved Raman subsystem

Time-resolved Raman scattering is an emerging and rapidly developing branch of Raman scattering. It presents us an alternative degree of freedom beyond temperature and magnetic field to look into Raman process. It can tell us the important information on the non-equilibrium dynamics of electrons or other excitations involved in Raman process. We can expect that the time-resolved technique under low temperatures and high magnetic fields will open a fascinating and unique window for exploring novel quantum phases.

There are different scenarios to realize time-resolved Raman scattering. A direct way is to excite the sample with a fast laser and collect Raman spectra with a high-speed gated detector synchronized with the excitation pulse. However, it is limited by available high-speed detectors and their sensitivity. Here we employ the standard pump-probe technique (Fig. 2). A key question for this technique is to get rid of the Raman signal excited by the pump. Surely one can separately produce the probe pulse, by using a CW laser with a mechanical high-speed chopper or a Q-switch laser. However, this will reach the time-scale ceiling in the ultrafast region (∼nanosecond).

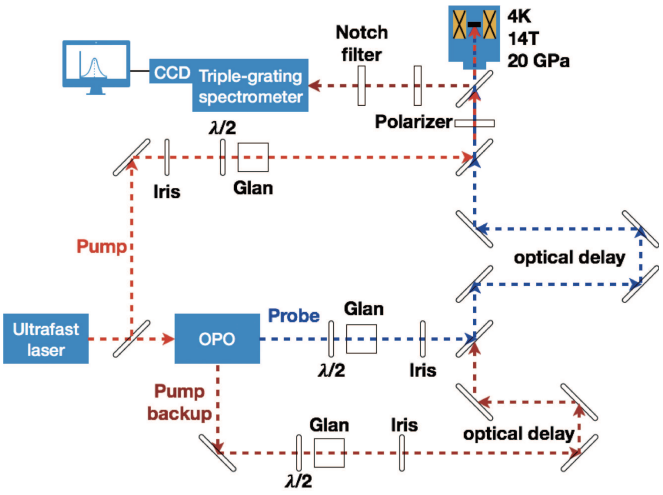


Fig. 2. (color online) Schematic diagram of time-resolved Raman scattering. Pump–probe technique is used here. Probe pulse is generated within an optical parameter oscillation (OPO) box and modulated by optical delay setup to realize the time delay from pump pulse. The idler light emitted out of OPO can be taken as a backup for pump sources.

In our case, the original intense pulse coming out of the ultrafast laser ($\sim$ 100 fs) is spilt into two beams by a 90/10 beam splitter. One beam is taken as the pump and the other as the probe after frequency-doubled in an OPO box. The large difference in frequency between the pump and probe allow us to clearly distinguish the Raman signal excited by the pump from the one by the probe. The orthogonal polarization configuration for the pump and the probe can further reduce the influence from the pump. The idler light emitted out of the OPO can be taken as a backup of pump sources, which effectively extends the frequency range of pump light. The optical delay setup consists of two motorized stages and two mirrors mounted on them. The programmable stages allow to be driven in a micrometer scale and hence can realize a precise time delay between the pump and probe (better than 50 fs).

Besides the ultrafast laser, the subsystem is also equipped with a broadband white light source developed very recently. It is particularly helpful for resonance studies. Therefore, we use the triple-grating spectrometer here (T64000), whose subtractive mode ideally matches the white light source.

Extreme conditions applied to this subsystem are quite similar to the ones for the CW Raman subsystem. Both systems have the similar optical inserts which is composed of many non-magnetic and low-thermal-expansion components like objective lens, precise XYZ stages and rotator. The maximum magnetic field here is 14 T rather than 9 T. It should be pointed out that high pressure up to 20 GPa is designed just to

be applied to CW measurements using white light source. At present it is not clear if high pressure cell can work well with time-resolved measurements, since the Raman signal may be extremely weak in this case.

2.3. Available measurement modes for Raman facility of SECUF

Now we can have a summary for the Raman facility. The extreme conditions applied to the facility include low temperature (4 K), high magnetic field (14 T), high pressure (20 GPa), and high time resolution (< 50 fs). In principles, one can combine one or more of these conditions to realize multi-dimensional Raman measurements and reveal novel condensed matter phases and excitations. According to the incident light source, the available Raman measurement modes can be divided into conventional CW Raman/photoluminescence mode, resonance mode and time-resolved mode. We put all these modes in the following table.

Table 1. Available measurement modes of SECUF Raman facility.

Measurement modes	Extreme conditions simultaneously available			
	Temperature/K	Magnetic fields/T	Pressure/GPa	Time resolution/ps
Conventional Raman/photoluminescence	4	9/14	20(LT)/100(RT)	–
Resonance Raman/photoluminescence	4	9/14	20(LT)/100(RT)	–
Time-resolved Raman/photoluminescence	4	9/14	–	< 50

3. Applications of Raman scattering under extreme conditions

Raman scattering has been proved to be an excellent method of characterizing the vibrational, electronic, and magnetic subsystems by probing the corresponding elementary excitations,[1,2] like phonon, magnon, electron, etc. The unique feature of this technique is that it can tell us symmetry, energy, and lifetime information about these excitations. When used in conjunction with pressure and magnetic field, Raman scattering can further provide pressure- and magnetic-field-dependent information about these excitations. These are proven valuable for understanding underlying physics and developing multiple applications. In the following we will present the applications of Raman scattering under high pressure and high magnetic field to a variety of condensed matter systems.

3.1. Pressure-induced phase transformations in Bromine and Iodine

Under compression most solids eventually undergo one or more structural phase transformations. The scope extends from drastic changes in volume, symmetry, and electronic properties to subtle shifts of lattice parameters. Raman scattering can catch the symmetry of a high-pressure phase through the assignment of new features and/or excitations. Thus, it has been widely applied to probe structural properties of solids under high pressures and to identify pressure-induced phase transitions.[3–6] A good example is to resolve pressure-induced successive structural changes in bromine (iodine).[7] Bromine shows a structural phase transformation from the molecular phase I to the intermediate phase V near 80 GPa (20 GPa for Iodine), and then to the monatomic phase II around 118 GPa (31 GPa for Iodine), as illustrated in Fig. 3(a).

Figures 3(b) and 3(c) show Raman spectra obtained for iodine and bromine up to 30 and 108 GPa, respectively. In the low-pressure region (< 20 GPa for iodine and < 80 GPa for bromine), the spectra have five distinct bands, originating from two librational modes ($A_g^{(L)}$, $B_{3g}^{(L)}$), two stretching modes ($A_g^{(S)}$, $B_{3g}^{(S)}$), and an unassigned X band. With increasing pressure Raman spectra drastically change and a new band grows up at 23 GPa for iodine (80 GPa for bromine). This new band originates neither from monatomic phase II nor from molecular phase I, because phase II has no Raman active band, and phase I has not shown any band in this low-frequency region. On the other hand, for the incommensurate intermediate phase V, there are two types of characteristic vibrational modes,[8] i.e., the amplitude mode (AMP, Fig. 3(a)) and the phase mode, and only the AMP mode is Raman active. Thus the new mode can be assigned to the AMP mode of phase V. This indicates a structural phase transformation from the molecular phase I to the intermediate phase V near 80 GPa for bromine (near 20 GPa for iodine).

The pressure dependence of the observed bands for iodine and bromine are shown in Figs. 4(a) and 4(b), respectively. The AMP modes show a softening behavior with increasing pressure and decreases to zero frequency at a critical pressure P_c. To estimate P_c, one can take a phenomenological function $\omega = (\omega_0^2 - aP)^{1/2}$ to fit the pressure dependence of the AMP mode frequencies. The fitting gives a P_c of 31 GPa for iodine (118 GPa for bromine). The zero frequency of AMP modes suggests another structural phase transformation from the intermediate phase V to the monatomic phase II near 118 GPa for bromine (near 31 GPa for iodine).

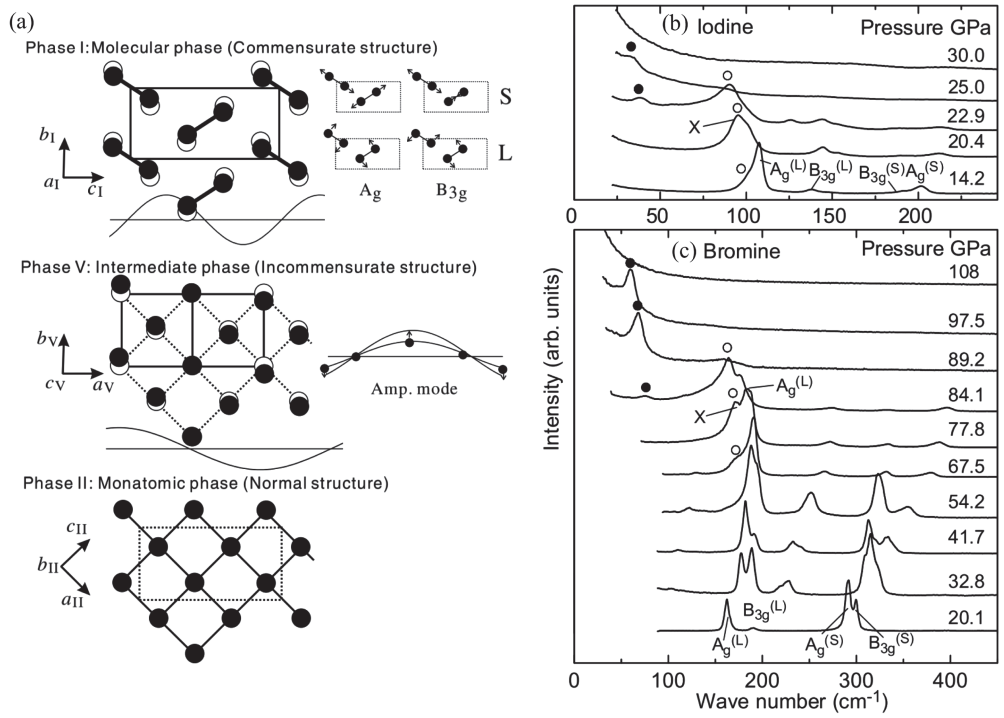


Fig. 3. (color online) (a) Crystal structures of three different phases. The open circles correspond to the parent structure without modulation (phase II). In phase I, there are two Raman active stretching ($A_g^{(S)}$, $B_{3g}^{(S)}$) and librational ($A_g^{(L)}$, $B_{3g}^{(L)}$) modes, while in phase V, only the amplitude (AMP) mode is Raman active. Raman spectra obtained for solid iodine up to 30 GPa (b) and for solid bromine up to 108 GPa (c), respectively. Open and closed circles correspond to X bands in phase I and new bands in phase V, respectively. Reprinted with permission from Ref. [7], copyright 2005 by the American Physical Society.

A more detailed discussion about the pressure-induced phase transformations in Bromine and Iodine is beyond the scope of this review, but the above results clearly demonstrate that Raman scattering is powerful to probe structural properties of solids under high pressures and to identify pressure-induced phase transitions.

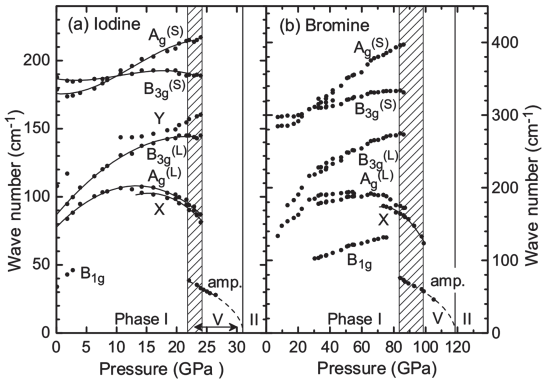


Fig. 4. Pressure dependence of vibrational frequencies of (a) solid iodine and (b) solid bromine, respectively. The dashed curves are the fitting results with a phenomenological function of $\omega = (\omega_0^2 - aP)^{1/2}$. A critical pressure P_c at $\omega = 0$ was obtained (31 and 118 GPa for iodine and bromine, respectively). Reprinted with permission from Ref. [7], copyright 2005 by the American Physical Society.

3.2. Pressure-tuned electronic transition in $Bi_{1.98}Sr_{2.06}Y_{0.68}Cu_2O_{8+\delta}$

In addition to the structural phase transition, pressure can also drastically alter the properties of the electronic subsystem and induce an electronic transition. This can be observed by electronic Raman scattering via light scattering from electronic fluctuations at Fermi surface. A nice demonstration is seen in $Bi_{1.98}Sr_{2.06}Y_{0.68}Cu_2O_{8+\delta}$,[9] a slightly doped ($\delta \sim 0.03$) and insulating parent compound of cuprates. Raman scattering studies reveal a pressure-tuned electronic phase transition at ~ 21 GPa.

Figure 5(a) shows Raman spectra of $Bi_{1.98}Sr_{2.06}Y_{0.68}Cu_2O_{8+\delta}$ at several pressures. The peaks at ~ 340, ~ 490, and ~ 620 cm^{-1} come from the out-of-phase vibrations of in-plane oxygen (B_{1g} "bond-buckling" mode), the oxygen vibration in the Bi–O block layer, and the vibration of apical oxygen.[10] The oxygen vibration in the block layers remains nearly constant with pressure, while B_{1g} and the apical oxygen modes shift by over ~ 100 cm^{-1}.

In general, Raman cross section is related to optical conductivity in the following way: $\chi''(\Omega) \propto \Omega\sigma'(\Omega)$, and thus a change in optical conductivity causes a change of low-frequency linear background of Raman cross section. Figure 5(b) shows a linear fit of electronic background, which exhibits a sharp step at ~ 21 GPa. Consistent with this change in the electronic background, electron–phonon coupling parameter λ (Fig. 5(c)) also shows a rapid increase at ~ 21 GPa. Furthermore, the ratio of integrated spectral weight of two-magnon peak (inset of Fig. 5(d)) has a similar behavior at ~ 21 GPa. The results indicate that an electronic phase transition in $Bi_{1.98}Sr_{2.06}Y_{0.68}Cu_2O_{8+\delta}$ occurs at ~ 21 GPa.

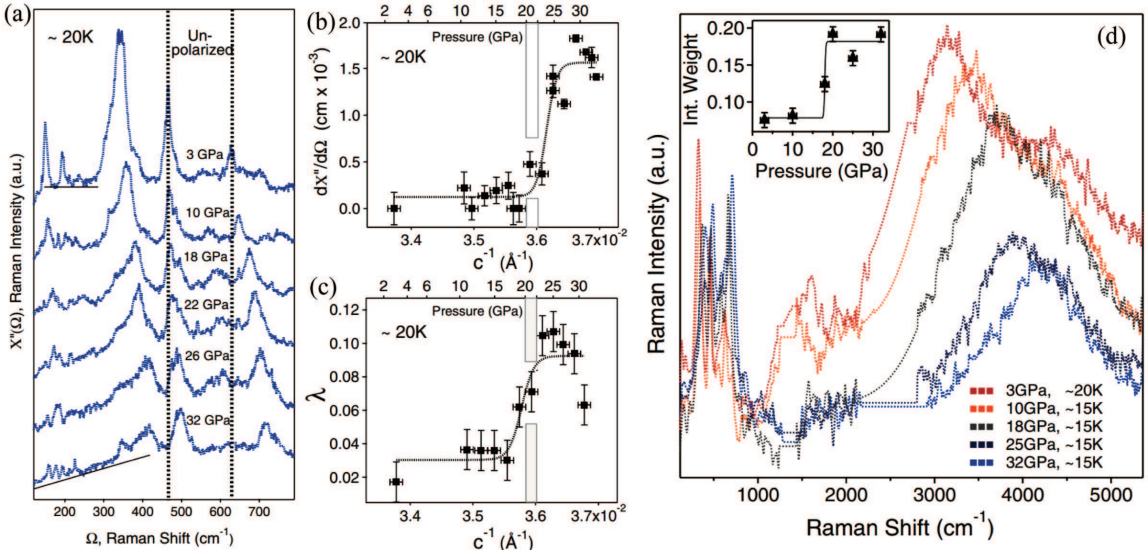


Fig. 5. (color online) (a) Raman spectra obtained at $\sim$ 20 K under pressure. (b) Slope of linear electronic background from 200–300 cm^{-1} at $\sim$ 20 K. Spectra under pressure were normalized to the intensity at 850 cm^{-1}. (c) Pressure dependence of electron–phonon coupling parameter λ obtained by fitting the B_{1g} phonon using the theory of Ref. [12]. (d) Raman spectra of two-magnon peak at $\sim$ 20 K under pressure. The inset is the ratio of the integrated spectral weight below 1000 cm^{-1} to that above 1000 cm^{-1} for each pressure. Reprinted with permission from Ref. [9], copyright 2008 by the American Physical Society.

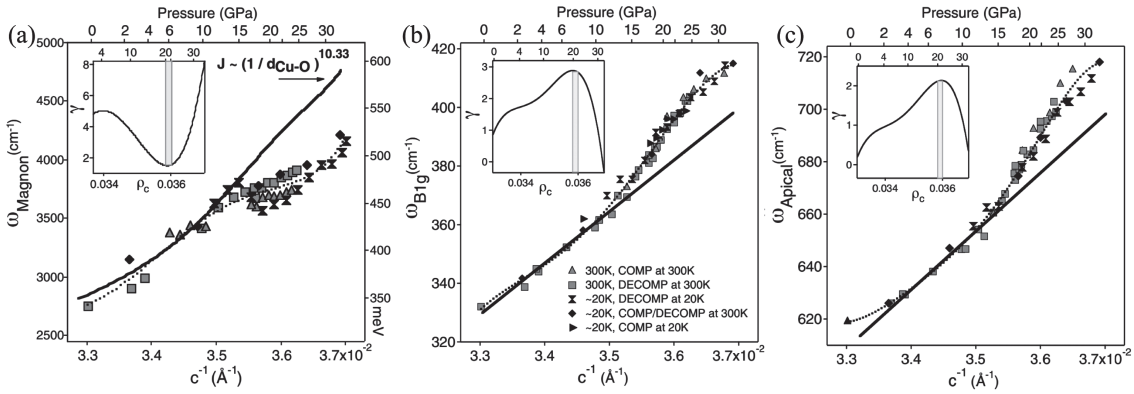


Fig. 6. (color online) Two-magnon peak positions (a), B_{1g} phonon frequencies (b), and apical phonon frequencies (c), at low (20 K) and high (300 K) temperatures versus the *c*-axis lattice density and pressure. The inset of panel (a) shows the derivative of fitting curve (dotted curve). Insets of panels (b) and (c) show the same derivative for phonons. Solid lines in panels (b) and (c) are guides to the eye, following the slope under low pressures. Reprinted with permission from Ref. [9], copyright 2008 by the American Physical Society.

On the other hand, two-magnon peak positions deviate from the power behavior $(1/d_{\mathrm{Cu-o}})^{\alpha}$ at $\sim$ 21 GPa (Fig. 6(a)), which has been observed in many other Mott–Hubbard insulators, such as K_2NiF_4.[11] The derivative of two-magnon peak positions has a minimum at $\sim$ 21 GPa (inset of Fig. 6(a)), which is consistent with the maximum of the Grüneisen parameter at $\sim$ 21 GPa (inset of Figs. 6(b) and 6(c)). These anomalous behaviors further support the electronic phase transition in $Bi_{1.98}Sr_{2.06}Y_{0.68}Cu_2O_{8+\delta}$ at $\sim$ 21 GPa.

The above example clearly demonstrates that electronic Raman scattering under high pressure is a sensitive probe for pressure-induced electronic phase transition.

3.3. Pressure-induced melting of charge density waves (CDW) in 1T-$TiSe_2$

In $Bi_{1.98}Sr_{2.06}Y_{0.68}Cu_2O_{8+\delta}$, electronic phase transition is evidenced by electronic Raman signals. In fact, electronic information can also be obtained through its coupling to the lattice, i.e., phonons, particularly for the systems involving a strong electron–lattice coupling. Numerous studies have been conducted in this aspect.[13–16] A good example is 1T-$TiSe_2$, which is a semimetal or small-gap semiconductor in the normal state and eventually develops into a commensurate CDW (inset of Fig. 7(a)) below a second-order phase transition near $T_{\mathrm{CDW}} \sim 200$ K.[13]

Figure 7(a) shows that the transition to CDW state in 1T-$TiSe_2$ results in several new modes, like E_g mode at $\sim$ 75 cm^{-1} and A_{1g} mode at $\sim$ 115 cm^{-1}. The two modes soften dramatically as the temperature increases toward CDW transition temperature, indicating that the two modes are CDW-related "amplitude" modes, denoted as E_g-CDW and A_{1g}-CDW, respectively. A_{1g}-CDW mode reflects the fluctuations of CDW amplitude that preserves the symmetry of CDW ground state, while E_g-CDW mode involves out-of-phase fluctuations of

CDW amplitude away from the ground-state symmetry. By tracking the pressure dependence of the mode energies, lifetimes, and intensities of the two phonons, one can get insight into the CDW state.

Figures 7(b)–7(d) show pressure-dependent Raman spectra of $TiSe_2$ at 3.5 K. The intensities of E_g-CDW and A_{1g}-CDW disappear above a critical pressure $P^* \sim 25$ kbar. The intensities of the modes serve as an order parameter of the CDW state, since CDW mode reflects fluctuations of the CDW state. The absence of the modes above P^* suggests that the CDW phase in 1T-$TiSe_2$ collapses above 25 kbar. A detailed pressure study of the energies and intensities of the two modes reveals more regimes about the CDW state.

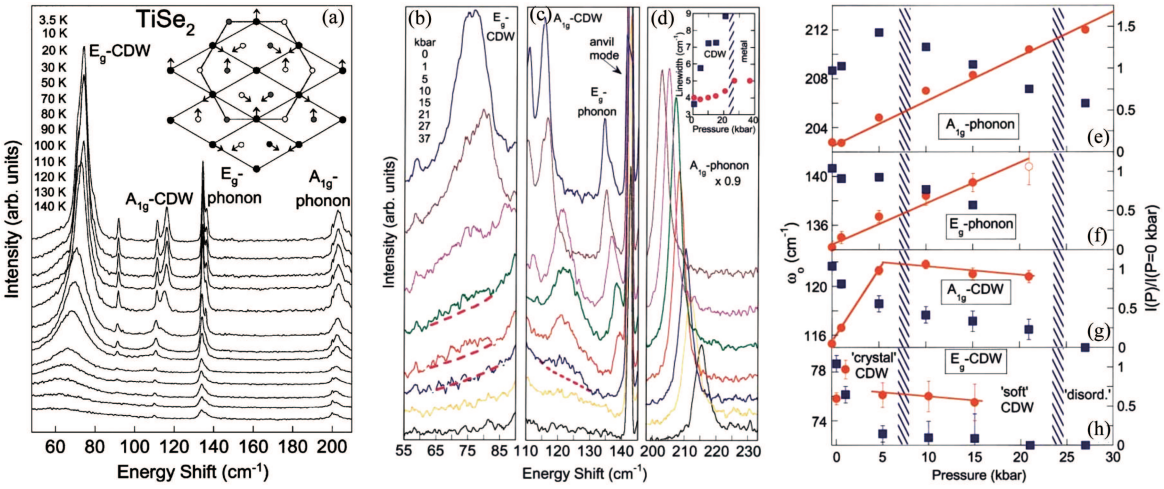


Fig. 7. (color online) (a) Temperature-dependent Raman spectra of $TiSe_2$. The inset shows the displacement pattern associated with the CDW distortion, for Ti atoms (solid circles), Se atoms above Ti layer (open circles), and Se atoms below Ti layer (shaded circles). Pressure dependence of Raman spectra at $T = 3.5$ K for E_g CDW mode (b), A_{1g} CDW and E_g optical phonon modes (c), and A_{1g} optical phonon mode (d). The inset of panel (d) shows the pressure dependence of A_{1g} (red circles) and A_{1g}-CDW (blue squares) phonon linewidths (FWHM). Pressure dependence of peak energies (circles) and normalized intensities, $I(P)/I(P=0)$ (squares) at $T = 3.5$ K for A_{1g} (e), E_g (f), A_{1g}-CDW (g), and E_g-CDW (h) modes. The hatched lines denote rough boundaries between crystalline CDW, soft CDW, and disordered CDW regimes. Reprinted with permission from Ref. [13], copyright 2003 by the American Physical Society.

(i) Crystalline CDW regime. From $P = 0$ to 5 kbar, the intensity of A_{1g}-CDW slightly decreases, but its energy increases linearly with increasing pressure. This is similar to that of 203 cm^{-1} and 134 cm^{-1} modes (Figs. 7(e) and 7(f)), indicating that the CDW state remains commensurate with the lattice in this regime.

(ii) Soft CDW regime. From $P = 5$ to 25 kbar, A_{1g}-CDW mode exhibits a softening with a rapid decrease in intensity and linewidth (inset of Fig. 7(d)). The behaviors are substantially different from that of 203 cm^{-1} and 134 cm^{-1} phonon modes (Figs. 7(e) and 7(f)), suggesting that the charge density wave becomes incommensurate in this pressure regime.

(iii) Disordered CDW regime. Above 25 kbar, both E_g-CDW and A_{1g}-CDW modes are completely suppressed, which means that the CDW state has melted into a metallic or semimetallic phase.

A detailed discussion on the pressure-induced phases of 1T-$TiSe_2$ is beyond the scope of this review. Anyway, the results shown here demonstrate that the Raman scattering high pressure is a powerful tool to study electronic phase transition through electron–phonon coupling.

3.4. Field-induced structural phase transition in Mn_3O_4

The application of magnetic field to Raman scattering allows us to study a lot of magnetic systems, particularly spin-lattice coupling systems. Magnetic-field-dependent Raman scattering has been widely used to study structural phase transitions.[17–23] Here a nice example is Mn_3O_4.[17] Raman scattering under magnetic fields offers field-dependent structural phase diagrams, and many microscopic details of field-dependent phase changes.

Mn_3O_4 has a spinel structure, $Mn^{2+}Mn_2^{3+}O_4$, which consists of two basic structural blocks, $Mn^{2+}O_4^{2-}$ tetrahedra and $Mn^{3+}O_6^{2-}$ octahedra (Fig. 8(a)). Below $T_c = 43$ K, Mn spins are ferrimagnetically ordered with Mn^{3+} spins antiparallel to [110] direction of tetrahedrally coordinated Mn^{2+} spins.[24] Below $T_2 = 33$ K, Mn_3O_4 has a commensurate spin structure, in which the net Mn spins are oriented along the [110] direction and the magnetic unit cell is doubled.[25] Figure 8(b) shows temperature dependence of ~ 295 cm^{-1} T_{2g} mode which is a triply degenerate mode associated with Mn–O bond-stretching vibrations of the ions at tetrahedral sites. From these spectra, one can find that T_{2g} mode splits into two modes near 290 cm^{-1} and 300 cm^{-1}. The splitting is consistent with a tetragonal-to-monoclinic distortion below $T_2 = 33$ K, which removes the degeneracy of T_{2g} mode. The distortion expands Mn^{2+}–O^{2-} bond length along the easy-axis [110] direction and decreases the energy for Mn–O vibrations in the [110] direction while it simultaneously contracts Mn^{2+}–

O^{2-} bond length along the easy-axis [1-10] direction and increases the energy for Mn–O vibrations along the direction. The high Raman intensity of the ~ 300 cm^{-1} mode suggests that the contracted Mn^{2+}–O^{2-} bonds are oriented in the direction of incident light polarization [1-10]. It can be expected that if the ~ 290 cm^{-1} mode has a higher intensity, the expanded Mn^{2+}–O^{2-} bond will be oriented along the [1-10] direction.

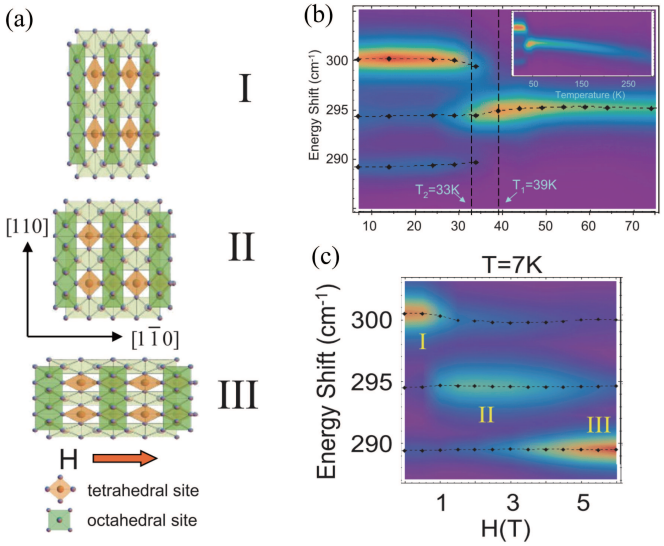


Fig. 8. (color online) (a) Crystal structure of Mn_3O_4 in the low-field monoclinic phase (top), intermediate undistorted tetragonal phase (middle), and high-field monoclinic phases (bottom). (b) Temperature dependence of T_{2g} Mn–O stretch mode, showing a mode splitting due to the removal of mode degeneracy from tetragonal II to monoclinic I transition. The inset shows an expanded view from 10 to 300 K. (c) Magnetic field dependence of T_{2g} mode at $T = 7$ K, showing the field-induced phase changes for $H \parallel$ [1-10]. Reprinted with permission from Ref. [17], copyright 2010 by the American Physical Society.

Figure 8 shows the field-dependent Raman spectra of Mn_3O_4 at $T = 7$ K and $H \parallel$ [1-10]. The ~ 300 cm^{-1} mode has a higher intensity below $H = 1$ T, while between 1 T and 4 T, the ~ 295 cm^{-1} T_{2g} mode appears with a high intensity. Above $H = 4$ T, the ~ 290 cm^{-1} mode has a higher intensity. The results indicate that with increasing magnetic fields along [1-10] direction, Mn_3O_4 undergoes a structural phase transformation from the monoclinic (structure I) to tetragonal phase (structure I) at ~ 1 T, and then to the monoclinic phase (structure III) at ~ 4 T. The major difference between structure I and structure III is that the structure I has an expanded Mn^{2+}–O^{2-} bond length along the [110] direction, while in structure III the expanded Mn^{2+}–O^{2-} bond length is along the [1-10] direction (Fig. 8(a)). Such a difference reflects structural response to the competition between the internal field and applied transverse field, which tend to align the Mn moments along the [110] and [1-10] directions, respectively.

3.5. Field dependence of electronic Raman scattering in overdoped $Tl_2Ba_2Cu_2O_{6+\delta}$

Electronic Raman scattering in metals results from electron–hole or multi-quasi-particle excitations around Fermi surface and may offer us charge and spin dynamics in different regions of Brillouin zone. For strongly correlated systems, incoherent quasiparticle scattering can usually lead to finite Raman intensity over a broad frequency range.[26,27] For the superconducting cuprates a flat continuum extending to at least 2 eV has been observed. On the other hand, the opening of a superconducting gap, $\Delta(\boldsymbol{k})$, will result in the so-called 2Δ/pair-breaking peak[28] in electronic Raman response due to the renormalization of the electronic continuum in the superconducting state. Thus, (i) the position of the 2Δ peak is proportional to a weighted average of the superconducting gap value; (ii) the peak intensity is proportional to the density of the superconducting condensate. When applying magnetic fields, Raman scattering can show us the field dependence of the 2Δ peak and get insight into the microscopic mechanism of superconductivity.[29–31] Here we will see a nice demonstration in overdoped $Tl_2Ba_2Cu_2O_{6+\delta}$.[29]

Figure 9(a) shows field-dependent Raman spectra of $Tl_2Ba_2Cu_2O_{6+\delta}$ at $T = 5$ K. The pair-breaking peak is

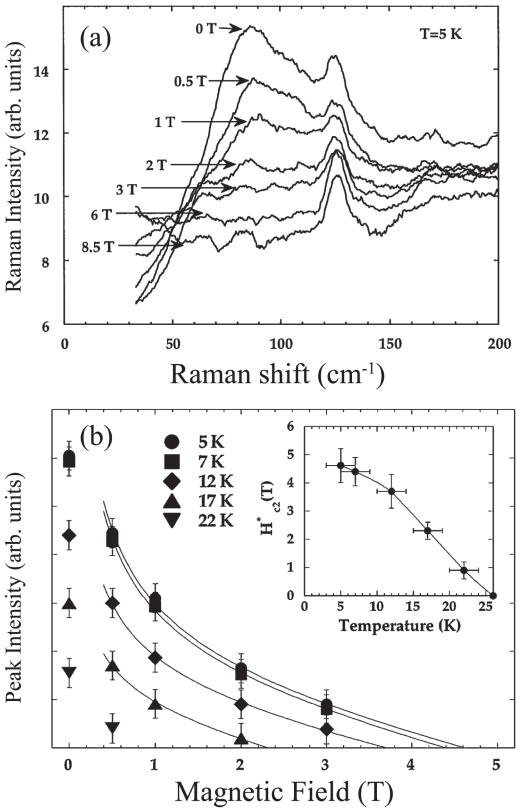


Fig. 9. (a) Magnetic field dependence of electronic Raman scattering response in the superconducting state of overdoped $Tl_2Ba_2Cu_2O_{6+\delta}$. Magnetic field clearly suppresses pair-breaking peak. (b) Field and temperature dependence of pair-breaking peak intensity. Inset: temperature dependence of upper critical field, $H^*_{c2}(T)$, obtained from Raman spectra. Reprinted with permission from Ref. [29], copyright 1997 by the American Physical Society.

substantially suppressed by magnetic fields, and gives a nonlinear field dependence (Fig. 9(b)). Blumberg *et al.*[29] attributed this behavior to a renormalization of density of states of quasiparticles near vortex cores. Through the field-dependent 2Δ-peak intensity at different temperature, one can obtain the effective critical field H^*_{c2} and its temperature dependence $H^*_{c2}(T)$ (inset of Fig. 9(b)). The temperature dependence is similar to that in the conventional superconductors, but in contrast to the anomalous temperature dependence of $H^*_{c2}(T)$ extracted from magnetoresistance measurements.[32,33]

3.6. Field-driven interaction between electronic excitations and phonons in $Co[N(CN)_2]_2$

Generally, external magnetic fields have two main effects that can be detected by Raman scattering. One is single spin effect, Zeeman splitting[34–36] and the other one is energy band effect, the formation of Landau levels.[37–39] Magnetic fields can continuously tune excitation energies and thus offer us an opportunity to manipulate multiple interactions. In the following we take Raman studies of $Co[N(CN)_2]_2$ under magnetic fields[34] as a good example.

Figure 10(a) displays magneto-Raman spectra of $Co[N(CN)_2]_2$ in the low-frequency range. The peaks near 147 and 158 cm^{-1} observed at zero field, originate from the wagging motions of Co-$N_{ax}C_{(2)}$ and Co-$N_{eq(2)}$. A new feature appears at $\sim$ 142 cm^{-1} at 15 T, and it grows with increasing magnetic fields by transferring intensities from the 147 and 158 cm^{-1} phonon modes. Its peak has a strong field dependence (Fig. 10(b)), pointing to either an electronic or magnetic origin. However, the position seems insensitive to Curie temperature ($\sim$ 9 K) (Fig. 10(c)). This excludes the scenarios involving magnons. The authors[34] assigned the feature as the Co^{2+} crystal-field excitation from the ground state Γ_6 level to the higher lying doublets of $^4T_{1g}$ term. The term moves with field as Zeeman effect comes into play (inset of Fig. 10(b)). Thus the following physical picture was proposed.

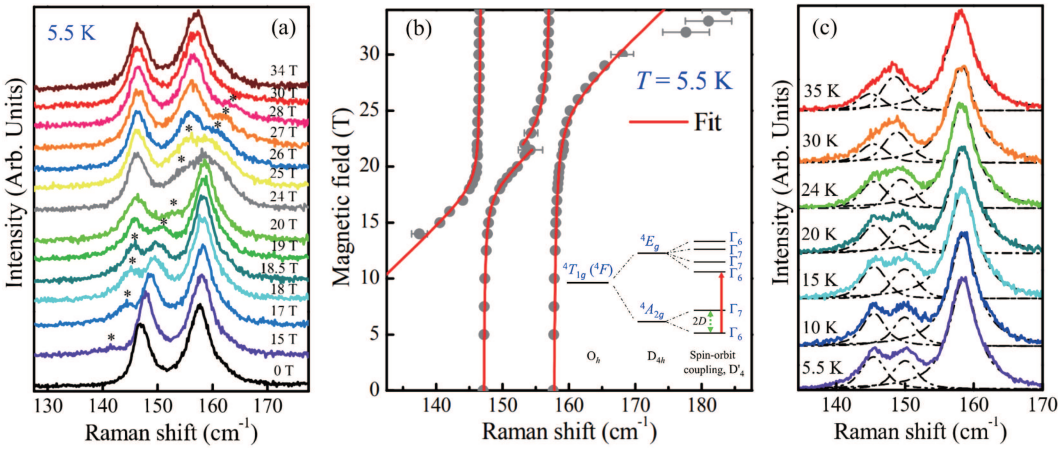


Fig. 10. (color online) (a) Magneto-Raman spectra of $Co[N(CN)_2]_2$ at $T = 5.5$ K under magnetic fields up to 34 T. The strong field-dependent feature, assigned as a Co^{2+} electronic excitation, is marked with an asterisk. (b) Raman shift versus applied fields, showing the hybridized electronic and phonon excitations in $Co[N(CN)_2]_2$. The red curves are fitting results using the theory of Ref. [36]. The inset shows a schematic energy level diagram for Co^{2+} electronic states. The red (solid) arrow shows a plausible candidate for the 114 ± 5 cm^{-1} excitation in Raman spectra. (c) Temperature dependence of magneto-Raman spectra at 18.6 ± 0.1 T. Black (dashed) lines are peak fits tracking the behavior of Co^{2+} electronic excitations, which displays no sensitivity to Curie temperature $\sim$ 9 K. Reprinted with permission from Ref. [34], copyright 2013 by the American Physical Society.

At 0 T, the intensity of the crystal-field excitation is too low to be observed, and there are only two phonons located at 147 and 158 cm^{-1}. The excitation energy continuously increases with increasing magnetic fields due to Zeeman splitting. When the excitation energy is close to 147 cm^{-1} phonon frequency, it will strongly interacts with the phonon mode and becomes observable by transferring intensity from the phonon mode. With further increasing magnetic fields, the electronic excitation moves close to and interacts with the second phonon mode, and repeats a similar behavior as the first one. In this process, the energies of the three modes can be well described by the crystal-field-phonon coupling theory (Fig. 10(b)).[36] At larger field, the energy of the electronic excitation is even bigger than that of the second phonon and becomes unobservable.

3.7. Pressure and field dependence of magnon scattering in $Ca_3Ru_2O_7$

In addition to the structural and electronic phase transition, Raman scattering is also an excellent technique for studying magnetic excitations,[40–44] including one- and two-magnon excitations. As a combined application of low temperatures, magnetic fields, and pressure to light scattering studies of magnons, here we consider $Ca_3Ru_2O_7$,[45,46] a bilayered, Ruddlesden-Popper-phase compound that exhibits a magnetic transition from a paramagnetic to an A-type antiferromagnetic state below $T_N = 56$ K, and a structural transition below $T_0 \sim 48$ K.

As shown in Fig. 11(a), below $T_N = 56$ K, a sharp peak appears near 56 cm^{-1} in Raman spectra of $Ca_3Ru_2O_7$. The

mode can be assigned as magnon scattering for the following reasons: (i) the magnon mode energy increases with decreasing temperature below T_N (Fig. 11(b)), reflecting the increase in $\langle S_z \rangle$ of Ru^{4+} spin with decreasing temperature; (ii) the magnon mode linewidth increases dramatically with increasing temperature below T_N, as observed in numerous different antiferromagnets;[48,49] (iii) the peak is observed only in the crossed scattering geometry $(z(x,y)\bar{z})$, consistent with theoretical expectations that magnon scattering involves off-diagonal terms in Raman tensors; (iv) the peak shows a clear Zeeman splitting when applied magnetic field $H \parallel ab$ plane (Fig. 12(b)).

Figure 11(c) shows the evolution of the magnon with pressure at 3.5 K and the pressure dependence of its frequency and linewidth is summarized in Fig. 11(d). Below $P = 46$ kbar, magnon frequency decreases with increasing pressure. This behavior is remarkably different from that observed in many Mott systems, in which magnon energy increases with increasing pressure.[50–52] The difference reflects a slight decrease in the zero-field magnon energy. The magnon mode disappears above $P = 46$ kbar, suggesting the collapse of the antiferromagnetic state in $Ca_3Ru_2O_7$.

More interestingly, Raman spectra of the magnon mode has an anisotropic magnetic field dependence, as shown in Fig. 12. The magnon mode energy is field-independent for $H \parallel c$ axis. However, for $H \parallel ab$ plane, the magnon mode shows a splitting and the splitting energy changes with magnetic field direction in ab plane (Figs. 12(c) and 12(d)). The splitting reaches its maximum for $H \parallel [110]$, suggesting that Ru spins are oriented at [110] direction (inset of Fig. 12(c)). The magnon modes collapse into a single mode at $H_c = 5.9$ T, suggesting a metamagnetic transition from A-type antiferromagnetic to ferromagnetic alignment.

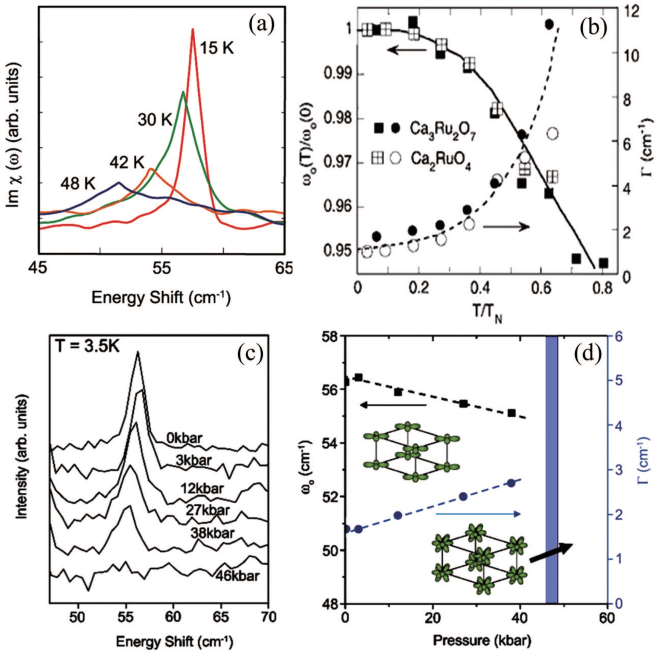


Fig. 11. (color online) (a) Temperature dependence of magnon scattering in $Ca_3Ru_2O_7$ ($T_N = 56$ K). (b) Normalized frequency, $\omega_o(T)/\omega_o(0)$ (squares), and linewidth, Γ (circles), as a function of normalized temperature, T/T_N. (c) Pressure dependence of magnon mode in $Ca_3Ru_2O_7$ at $T = 3.5$ K. (d) Magnon mode frequency (ω_o) and linewidth (Γ) versus pressure, and evidence for a pressure-induced phase change above 46 kbar where no magnon scattering is observed. Reprinted with permission from Refs. [45] and [46], copyright 2006 by the American Physical Society.

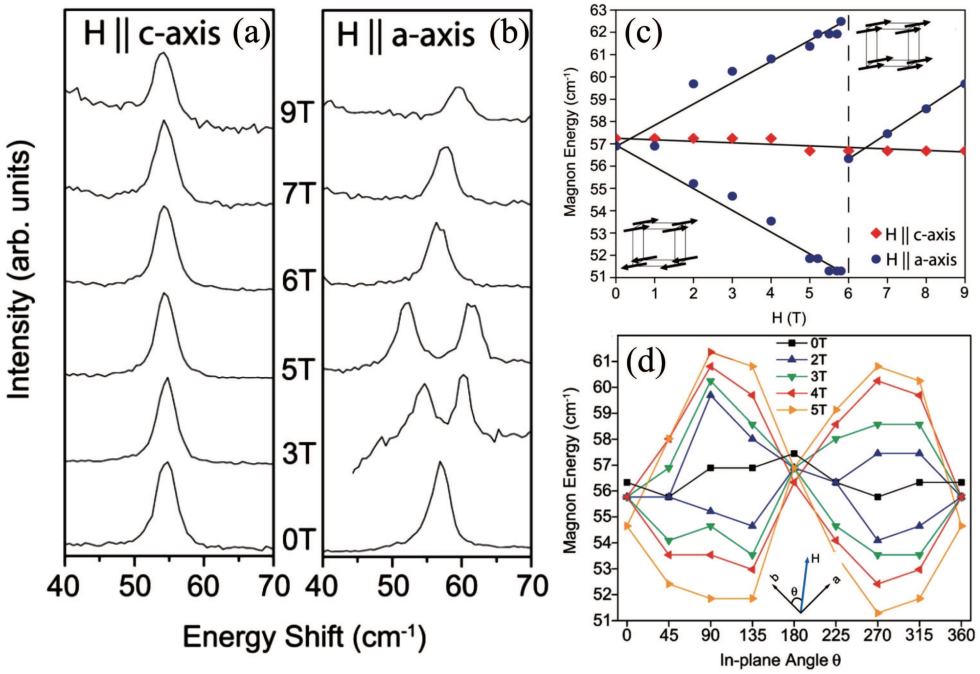


Fig. 12. (color online) Magnon scattering spectra of $Ca_3Ru_2O_7$ at $T = 11.5$ K under applied magnetic fields parallel to the c-axis (a) and the a-axis (b). (c) Magnon energies versus magnetic fields for $H \parallel c$-axis (red diamonds) and $H \parallel a$-axis (blue circles). (d) Magnon energy in $Ca_3Ru_2O_7$ as a function of magnetic-field orientations at $T = 11.5$ K. Reprinted with permission from Refs. [45] and [46], copyright 2006 by the American Physical Society.

4. Time-resolved Raman spectroscopy

4.1. Ultrafast photo-induced structure phase transition in antimony

The interplay between different excitations in condensed matter, like phonons, magnons, electron–hole excitations, etc., plays a crucial role in determining their physical properties. Optically induced excitations typically leads to the creation of excited electron–hole pairs, which relax to a thermal equilibrium state in a fast time scale. For a modest level of optically induced excitations, the process of electron–hole excitation and subsequent relaxation can be considered as a near-equilibrium phenomenon and the structural and electronic properties of materials do not change much. However, optically induced phase transitions may occur if the density of optically induced excitations is high enough. Here we will discuss an example, A7 semimetal antimony,[53] which undergoes a structural phase transition when the pump excitation density exceeds 5 mJ/cm^2.

Most elemental metals crystallize into a cubic or hexagonal closed structure. Crystalline Sb may be described as a distorted simple cubic structure (Fig. 13(a)). The unusual structure stems from strong electron–phonon coupling in antimony. In one dimension, this type of distortion is the well-known Peierls distortion. As shown in Fig. 13(a), the distortion will open a gap at Fermi level and reduce the energy of electronic subsystem. The energy cost due to the structural distortion is compensated by the electronic energy gain and results in a net energy gain. Therefore, it is expected that a sufficiently high occupation of conduction band, realized by photo-excitation, will lead to a recovery of the undistorted cubic structure. The idea can be well examined by time-resolved Raman experiment, where the pump light is used to stimulate valence-band electrons and the structural information is detected through the probe light.

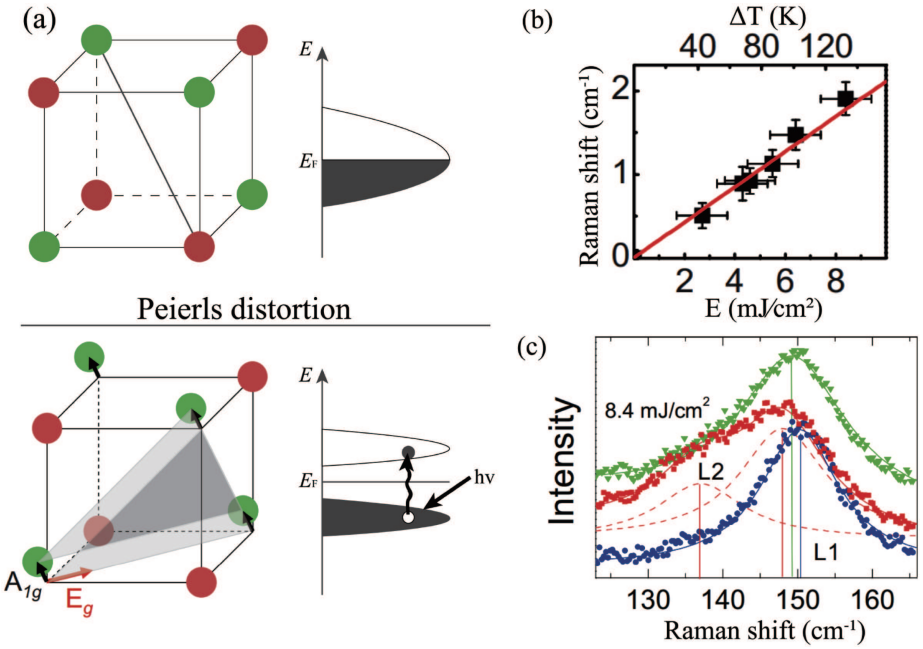


Fig. 13. (color online) (a) Structure of A7 semimetals and photo-induced reversed Peierls transition. Photo-excitation reduces the population of valence bands, hence reducing the electronic energy gain of Peierls distortion, and driving the system toward the undistorted phase. (b) A_{1g} phonon frequency in Sb measured at 15 ps after photo-excitation. The agreement between the model and the data indicates that electronic heat diffusion plays a minor role in the relaxation processes. (c) The symmetry reduction due to the photo-induced phase transition leads to the emergence of an additional phonon mode on the low-energy side of A_g mode for excitation densities larger than 5 mJ/cm^2. Reprinted with permission from Ref. [53], copyright 2009 by the American Physical Society.

The difference between A7 and "cubic" structures is that (111) plane of A7 structure has an alternating displacement along the [111] direction. This corresponds to Raman active A_{1g} phonon mode (Fig. 13(a)), whose frequency is linearly proportional to the applied optical pump excitation density (Fig. 13(b)). The behavior is consistent with the calculated temperature dependence of this phonon frequency.[54] More interestingly, a second mode is observed under the excitation density of pump laser exceeding 5 mJ/cm^2 (L2, Fig. 13(c)). The new mode reflects an optically induced structural phase transition. Surprisingly, the induced phase is not the expected simple cubic structure since there is no optical phonon in this structure, but rather a phase with symmetry lower than A7 structure. The observations suggest that the photo-induced phase might be understood in terms of an additional E_g distortion.

4.2. Quasiparticle dynamics in high-temperature superconductors $Bi_2Sr_2CaCu_2O_{8+\delta}$

One of the most intriguing open problems in condensed matter is the origin of high-temperature superconductivity. So far, the superconducting phase has been widely studied

at thermal equilibrium through numerous techniques. However, few experiments have been performed to investigate their non-equilibrium properties. The development of Ti:Sapphire pulsed laser makes it possible. It was proposed that time-resolved Raman spectroscopy can be employed to probe the non-equilibrium properties of high-temperature superconductors (HTSCs).[55–57] The non-equilibrium properties in the superconducting phase has been first reported by Saichu *et al.*[55] They studied the superconducting order parameter in slightly over-doped $Bi_2Sr_2CaCu_2O_{8+\delta}$(Bi-2212, $T_c = 82$ K) and found two different coupling mechanisms that contribute equally to the pair-breaking peak.

Figure 14(a) displays Bose-factor-corrected steady state spectra between 100 and 600 cm^{-1} in the normal and superconducting state of Bi-2212. In the normal state one can see a flat background, while in the superconducting state a pair-breaking peak develops at ~ 420 cm$^{-1} \simeq 52$ meV, which is the so-called 2Δ peak. Figure 14(b) displays three differential Raman spectra (i.e., $I^{1.65}(\omega) - I^{0}(\omega)$) at 10 K as a function of delay time between pump and probe pulses. The contour plot of differential spectra are shown in Fig. 14(c). The high-energy wing of pair-breaking peak (above the dashed line in Fig. 14(c)) shows a fast decrease (2 ps), while the low-energy spectral weight (100–200 cm^{-1}) increases at roughly 3 ps, reflecting a spectral weight transfer from the pair-breaking peak to the sub-gap region upon photo-excitation. However, a closer observation leads one to conclude that the relaxation of the non-equilibrium state occurs in a nontrivial way and can be divided into two stages.

(i) The high-energy part of pair-breaking peak ($\sim$ 420–600 cm^{-1}, above the dashed line in Fig. 14(c)), shows a fast (2 ps) decrease followed by a slow relaxation (7.4 ps). Saichu *et al.* suggested that this decay may be related to hole–phonon coupling via in-plane breathing mode.

(ii) At the same time, the low-energy part of pair-breaking peak ($\sim$ 220–420 cm^{-1} in Fig. 14(c)) starts to decay at 5 ps after photo-excitation, followed by a fast relaxation (1.4 ps). The authors argued that this behavior might be understood by a second coupling mechanism arising from hole–spin coupling.

The work by Saichu *et al.*[55] have demonstrated that time-resolved Raman spectroscopy is an effective tool to probe the non-equilibrium electronic properties of HTSCs and shed light on the origin of superconductivity.

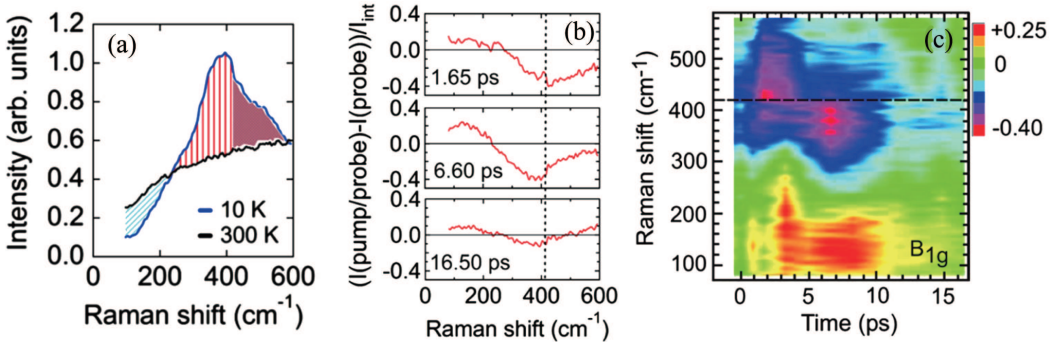


Fig. 14. (color online) (a) Steady-state Raman spectra of $Bi_2Sr_2CaCu_2O_{8+\delta}$ in B_{1g} geometry (in Porto notation $z(xy)z$, where z is perpendicular to the CuO planes) at 10 and 300 K. A gap opens below 250 cm^{-1} (blue area) and a pair-breaking peak appears around 420 cm^{-1} (red area). (b), (c) Temporal evolution of time-resolved differential Raman spectra at 10 K in B_{1g} geometry. Three differential spectra at three delay times are shown in panel (b), while a contour plot consisting of 12 differential Raman spectra is presented in panel (c). The dashed line separates pair-breaking peak into two energy regions that have distinct characteristic behaviors. The change in intensity is colored. There is a transfer of spectral weight from high to low energies after 1 ps. Reprinted with permission from Ref. [55], copyright 2009 by the American Physical Society.

5. Summary

In this review, we have presented a brief introduction to Raman scattering, followed by a detailed description of the Raman facility belonging to the SECUF, including the system design and the capability the facility can provide. We have demonstrated that Raman scattering under extreme conditions (e.g., low temperature, high magnetic field, and high pressure), can effectively detect many elementary excitations including electron, phonon, magnon, etc., in a variety of correlated electron systems. The present review offers a glimpse of SECUF Raman facility and its possible applications. We hope that this may stimulate increased and multidisciplinary collaborations based on the facility in the future.

References

[1] Devereaux T P and Hackl R 2007 *Rev. Mod. Phys.* **79** 175
[2] Lemmens P, Güntherodt G and Gros C 2003 *Phys. Rep.* **375** 1
[3] Goncharov A F 2012 *International Journal of Spectroscopy* **2012** 1
[4] Goncharov A F and Struzhkin V V 2003 *J. Raman Spectrosc.* **34** 532
[5] Lucazeau G 2003 *J. Raman Spectrosc.* **34** 478
[6] Gillet P 1996 *Phys. Chem. Miner.* **23** 263
[7] Kume T, Hiraoka T, Ohya Y, Sasaki S and Shimizu H 2005 *Phys. Rev. Lett.* **94** 065506
[8] Cummins H Z 1990 *Phys. Rep.* **185** 211
[9] Cuk T, Struzhkin V V, Devereaux T P, Goncharov A F, Kendziora C A, Eisaki H, Mao H K and Shen Z X 2008 *Phys. Rev. Lett.* **100** 217003
[10] Kakihana M, Osada M, Käll M, Börjesson L, Mazaki H, Yasuoka H, Yashima M and Yoshimure M 1996 *Phys. Rev. B* **53** 11796
[11] Struzhkin V V, Schwarz U, Wilhelm H and Syassen K 1993 *Mater. Sci. Eng. A* **168** 103
[12] Devereaux T P, Virosztek A and Zawadowski A 1995 *Phys. Rev. B* **51** 505

[13] Snow C S, Karpus J F, Cooper S L, Kidd T E and Chiang T C 2003 *Phys. Rev. Lett.* **91** 136402

[14] Bera A, Pal K, Muthu D V S, Sen S, Guptasarma P, Waghmare U V and Sood A K 2013 *Phys. Rev. Lett.* **110** 107401

[15] Nayak A P, Bhattacharyya S, Zhu J, Liu J, Wu X, Pandey T, Jin C, Singh A K, Akinwande D and Lin J F 2014 *Nat. Commun.* **22** 087407

[16] McWhan D B, Fleming R M, Moncton D E and DiSalvo F J 1980 *Phys. Rev. Lett.* **45** 269

[17] Kim M, Chen X M, Joe Y I, Fradkin E, Abbamonte P and Cooper S L 2010 *Phys. Rev. Lett.* **104** 136402

[18] Byrum T, Gleason S L, Thaler A, Macdougall G J and Cooper S L 2016 *Phys. Rev. B* **93** 184418

[19] Gleason S L, Byrum T, Gim Y, Thaler A, Abbamonte P, Macdougall G J, Martin L W, Zhou H D and Cooper S L 2014 *Phys. Rev. B* **89** 134402

[20] Rovillain P, Cazayous M, Gallais Y, Measson M A, Sacuto A, Sakata H and Mochizuki M 2011 *Phys. Rev. Lett.* **107** 027202

[21] Kim M, Chen X M, Wang X, Nelson C S, Budakian R, Abbamonte P and Cooper S L 2011 *Phys. Rev. B* **84** 174424

[22] Ji J T, Zhang A M, Xia T L, Cao Q, Liu G L, Hou D and Zhang Q M 2010 *Phys. Rev. B* **82** 014408

[23] Faugeras C, Kossacki P, Basko D M, Amado M, Sprinkle M, Berger C, De Heer W A and Potemski M 2010 *Phys. Rev. B* **81** 155436

[24] Chung J H, Kim J H, Lee S H, Sato T J, Suzuki T, Katsumura M and Katsufuji T 2008 *Phys. Rev. B* **77** 054412

[25] Jensen G B and Nielsen O V 1974 *J. Phys. C* **7** 409

[26] Varma C M, Littlewood P B, Schmitt-Rink S, Abrahams E and Ruckenstein A E 1989 *Phys. Rev. Lett.* **63** 1996

[27] Shastry B S and Shraiman B I 1990 *Phys. Rev. Lett.* **65** 1068

[28] Cooper S L, Klein M V, Pazol B G, Rice J P and Ginsberg D M 1988 *Phys. Rev. B* **37** 5920

[29] Blumberg G, Kang M and Klein M V 1997 *Phys. Rev. Lett.* **78** 2461

[30] Qazilbash M M, Koitzsch A, Dennis B S, Gozar A, Balci H, Kendziora C A, Greene R L and Blumberg G 2005 *Phys. Rev. B* **72** 214510

[31] Geng Z H 2014 *Phys. Lett. A* **378** 1309

[32] Dalichaouch Y, Lee B W, Seaman C L, Markert J T and Maple M B 1990 *Phys. Rev. Lett.* **64** 599

[33] Mackenzie A P, Julian S R, Lonzarich G G, Carrington A, Hughes S D, Liu R S and Sinclair D C 1993 *Phys. Rev. Lett.* **71** 1238

[34] Brinzari T V, Haraldsen J T, Chen P, Sun Q C, Kim Y, Tung L C, Litvinchuk A P, Schlueter J A, Smirnov D, Manson J L, Singleton J and Musfeldt J L 2013 *Phys. Rev. Lett.* **111** 047202

[35] Strach T, Ruf T, Cardona M, Jandl S, Nekvasil V, Chen C, Wanklyn B M, Zhigunov D I, Barilo S N and Shiryaev S V 1997 *Phys. Rev. B* **56** 5578

[36] Ruf T, Heyen E T, Cardona M, Mesot J and Furrer A 1992 *Phys. Rev. B* **46** 11792

[37] Perreault B, Rachel S, Burnell F J and Knolle J 2017 *Phys. Rev. B* **95** 184429

[38] Henni Y, Ojeda Collado H P, Nogajewski K, Molas M R, Usaj G, Balseiro C A, Orlita M, Potemski M and Faugeras C 1992 *Nano Lett.* **16** 3710

[39] García-Flores A F, Terashita H, Granado E and Kopelevich Y 2009 *Phys. Rev. B* **79** 113105

[40] Sethi A, Byrum T, McAuliffe R D, Gleason S L, Slimak J E, Shoemaker D P and Cooper S L 2017 *Phys. Rev. B* **95** 174413

[41] Mallett B P P, Wolf T, Gilioli E, Licci F, Williams G V M, Kaiser A B, Ashcroft N W, Suresh N and Tallon J L 2013 *Phys. Rev. Lett.* **111** 237001

[42] Cazayous M, Gallais Y, Sacuto A, De Sousa R, Lebeugle D and Colson D 2008 *Phys. Rev. Lett.* **101** 037601

[43] Kuroe H, Kusakabe K, Oosawa A, Sekine T, Yamada F, Tanaka H and Matsumoto M 2008 *Phys. Rev. B* **77** 134420

[44] Struzhkin V V, Goncharov A F, Mao H K, Hemley R J, Moore S W, Graybeal J M, Sarrao J and Fisk Z 2000 *Phys. Rev. B* **62** 3895

[45] Karpus J F, Snow C S, Gupta R, Barath H, Cooper S L and Cao G 2006 *Phys. Rev. B* **73** 134407

[46] Snow C S, Cooper S L, Cao G, Crow J E, Fukazawa H, Nakatsuji S and Maeno Y 2002 *Phys. Rev. Lett.* **89** 226401

[47] Gupta R, Kim M, Barath H, Cooper S L and Cao G 2006 *Phys. Rev. Lett.* **96** 067004

[48] Fleury P A and Loudon R 1968 *Phys Rev.* **166** 514

[49] Sugai S, Sato M, Kobayashi T, Akimitsu J, Ito T, Takagi H, Uchida S, Hosoya S, Kajitani T and Fukuda T 1990 *Phys. Rev. B* **42** 1045

[50] Aronson M C, Dierker S B, Dennis B S, Cheong S W and Fisk Z 1991 *Phys. Rev. B* **44** 4657

[51] Katano S, Môri N, Takahashi H and Takei H 1989 *J. Phys. Soc. Jpn.* **58** 3890

[52] Massey M J, Chen N H, Allen J W and Merlin R 1990 *Phys. Rev. B* **42** 8776

[53] Fausti D, Misochko O V and Van Loosdrecht P H M 2009 *Phys. Rev. B* **80** 161207

[54] Wang X, Kunc K, Loa I, Schwarz U and Syassen K 2006 *Phys. Rev. B* **74** 134305

[55] Saichu R P, Mahns I, Goos A, Binder S, May P, Singer S G, Schulz B, Rusydi A, Unterhinninghofen J, Manske D, Guptasarma P, Williamsen M S and Rübhausen M 2009 *Phys. Rev. Lett.* **102** 177004

[56] Machtoub L, El Machtoub G, Shimoyama J, Suemoto T and Kishio K 2003 *Physica C* **392** 291

[57] Machtoub L H, Suemoto T, Shimoyama J and Kishio K 2002 *J. Raman Spectrosc.* **33** 471